Active Model-Based Fault Diagnosis in Reconfigurable Battery Systems

Michael Schmid, Emanuel Gebauer, Christian Hanzl, and Christian Endisch, *Member, IEEE*

***Abstract*—With the increasing demand for electric vehicles, the interest in battery systems is growing. In order to enable safe operation of these complex energy storage systems, methods of fault diagnosis are needed. Particularly, reconfigurable battery systems (RBSs) with switches are promising on the way to fault tolerance as they allow the system to be reconfigured in the event of a fault. In this article, a model-based fault diagnosis algorithm is developed and validated that uses the switches of an RBS to improve the fault isolability. Since the algorithm changes the structure of the system in order to differentiate between nonisolable faults, it is classified as an active fault diagnosis algorithm. The deviations between sensor measurements and model, called residuals, are stochastically analyzed. For fault isolation, a fuzzy clustering approach is used. A constrained sigma-point Kalman filter minimizes model uncertainties and therefore increases the sensitivity and robustness of the fault diagnosis approach. Furthermore, the filter allows estimating the fault amplitude in case of a fault. Based on active sequential hypothesis testing, a policy to calculate the next switch position is proposed and investigated. It is shown simulatively and experimentally that additional faults are isolated by the presented active approach.**

***Index Terms*—Active fault isolation, active hypothesis testing, constrained parameter estimation, fault tolerance, fuzzy clustering, reconfigurable battery system (RBS).**

I. Introduction

ELECTRIC vehicles play a key role in achieving the climate goal of keeping the increase in global average temperature below 1.5 °C. Especially in electric vehicles, large battery packs are used to meet the power and range requirements. Such battery systems are complex and require a high degree of uniformity and reliability of the individual cells. Recently, more and more reconfigurable battery systems (RBSs) with switches [1]–[3] and battery management systems (BMS) with single-cell monitoring [4] have received attention, as they are a promising way to alleviate the uniformity requirements for single cells. The monitoring includes preventing overcharging, undercharging and overheating. In addition, BMS that follow the standard formulated by the International Electrotechnical Commission provide a fault diagnosis that is able to detect certain faults in the system. It includes an early alarm of unhealthy cells and information of the battery aging [5], [6].

Faulty cells in a large-scale battery system cause a serious risk to the surroundings [7]. Even minor faults, such as an increased contact resistance, result in inefficient system operation and increased heat generation [8]. Therefore, fault diagnosis is a crucial part in a battery system, ensuring longevity and safety throughout the whole operating time. Fault diagnosis can be divided into four subtasks. Fault detection refers to the discovery of a fault. Fault isolation involves the localization or classification of the fault. Fault analysis or identification refers to the determination of the magnitude and cause of the fault. Based on this, fault tolerance allows a continuation of the operation. In RBS, fault tolerance can be achieved, for example, by reconstructing a faulty sensor signal [9], [10], or by bypassing a cell [2], [11]. If, for example, an internally short-circuited cell is electrically isolated from the cells connected in parallel to it, the switches of the RBS prevent the defective cell from being supplied by an additional current. The prevention of feeding neighboring cells with additional energy is particularly promising to prevent thermal runaway propagation.

In model-based fault detection and isolation (FDI), the difference between the real physical system and a computational model is analyzed. In the following, we will differentiate between passive and active *FDI*. The former only analyzes the measurements of the system as an external observer, whereas the latter extends this analysis by choosing actions on the system in order to further improve the fault diagnosis. First, the state of the art in the literature on passive *FDI* is presented. Based on structural analysis, minimal structurally overdetermined (MSO) subsets can be used to generate residuals for fault diagnosis [12], [13]. Zheng *et al.* [14] diagnose faults in voltage and current measurements using an unscented particle filter. Dey *et al.* [15] solve this task using sliding mode observers based on the electrical and thermal dynamics of the battery system. To obtain a robust estimate of the state of energy, an observer-based current sensor fault diagnosis is performed in [16]. In [17], the voltage and current sensor faults are detected by the difference between the true state-of-charge (SoC) and the estimated SoC of each cell. Liu and He [18] have proposed an approach for sensor fault diagnosis in which the two cells with the highest voltage and the lowest voltage are observed with an adaptive extended Kalman filter (EKF). It is assumed that the two observed cells are the cells most likely to be over- or undercharged. The remaining cells are monitored offline with a long time interval. Based on

Manuscript received March 22, 2020; revised May 29, 2020 and June 24, 2020; accepted July 25, 2020. Date of publication July 30, 2020; date of current version October 30, 2020. This work was supported by the AUDI AG. Recommended for publication by Associate Editor S. Williamson. *(Corresponding author: Michael Schmid.)*

The authors are with the Institute of Innovative Mobility, Technische Hochschule Ingolstadt, 85049 Ingolstadt, Germany (e-mail: michael.schmid@thi.de; emanuel.gebauer@thi.de; christian.hanzl@thi.de; christian.endisch@thi.de).

Color versions of one or more of the figures in this article are available online at https://ieeexplore.ieee.org.

Digital Object Identifier 10.1109/TPEL.2020.3012964

a system identification using the recursive least squares method and an EKF, Chen *et al.* [19] present an approach to voltage fault detection. A degree of anomaly, the local outlier factor, is calculated and evaluated using an outlier filter based on Grubbs criterion. In [20], a Luenberger observer is used for the fault isolation and estimation of an increased internal resistance in serially connected battery cells. The actions of *active FDI* approaches can include adding an auxiliary input to the system as in [21] and [22] or (as in our case) changing the structure of the battery system via switches in RBS. In this article, a novel method for active hypothesis testing based on previous investigations by [23]–[26] is introduced. Chernoff [23] introduced a policy to test $|\mathbb{H}| = 2$ different hypotheses $\mathcal{H}_1, \mathcal{H}_2 \in \mathbb{H}$ that are uniquely distinguishable for all actions and showed its asymptotic optimality ($L \to \infty$) for the cost L of making a wrong declaration. Nitinawarat *et al.* [24] and Naghshvar and Javidi [25], [26] generalized their approach, alleviated the need for distinguishability and allowed to test multiple hypothesis ($|\mathbb{H}| > 2$). Cohen and Zhao [27] used active hypothesis testing for anomaly detection. The aim is to find the root cause of a fault by successively choosing a measurement subspace and evaluating whether these measurements indicate an anomaly in the measured subsystem or not. By repeating this procedure, Cohen and Zhao [27] were able to isolate their anomalies.

The aforementioned approaches to model-based fault diagnosis [13]–[20] have one or more of the following issues. They are applied to a single cell [13], [15], [16] or serially connected cells [17], [19], [20] with the assumption that cells connected in parallel behave like one large cell. This neglects the current distribution of paralleled cells as well as contact and busbar resistances. While in previous literature often only sensor faults are considered [13]–[19], in this article both sensor and parameter faults for a connection of several battery cells are considered. None of the model-based approaches has been applied to RBS to diagnose electronic faults in addition to cell faults. In particular, the model-based approaches presented have in common that they use the sensor measurements in a passive way and do not actively reconfigure the battery system for fault diagnosis. To the authors' best knowledge, FDI in RBS has not been investigated previously. The aforementioned approaches to active fault diagnosis [21], [22] also pose challenges when applied in battery systems. The load profile is determined by the operation of the vehicle, therefore an additional excitation is accompanied by additional losses. The approaches [23]–[27] have in common that the decision is based on comparing the probability density function (PDF) of the residuals after the action, called kernels, assuming each hypothesis is true. These kernels however are generally unknown and hard to estimate, as they heavily depend on the fault amplitude. Fast varying fault amplitudes and the uncertainty about the true fault in the system further complicate the estimation of the kernels. This is taken as a motivation to develop an active hypothesis testing policy based on [25] without the need of knowledge about the fault amplitude.

To address the mentioned issues, a framework for active FDI is presented that uses the switches of an RBS to isolate between faults. The main contribution of this article is summarized as follows.

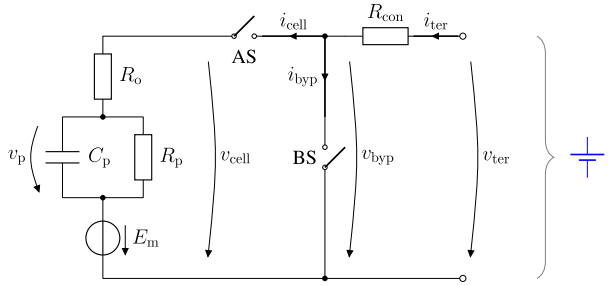

Fig. 1. RBS cell (blue): Single *RC*-model of one Li-ion cell with an active switch (AS) and a bypass switch (BS). R_{con} is the contact resistance between the cell terminal and the busbar.

1) An analytic measure for detectability is introduced in order to account for changes in the detectability of a fault for different switch positions.
2) The proposed approach considers both parameter and sensor faults inside and outside each battery cell in a 2s3p module.
3) An approach for active FDI in an RBS is presented. A novel adaptive sequential active hypothesis testing policy based on [25] is presented, that is independent of the fault amplitude.

The remainder of this article is organized as follows. In Section II, the electrical models for one single cell in the RBS and for the interconnection of six RBS cells are presented. Based on the model, the implemented residuals for fault diagnosis are discussed (see Section III). A constrained parameter estimator is used to adapt the model parameters to the experimental setup in order to improve the sensitivity of the fault diagnosis algorithm and estimate the fault amplitude. In Section IV, the residuals are analyzed stochastically. A fuzzy clustering approach is used for fault isolation. In addition, active fault diagnosis based on active hypothesis testing and a detectability measure are presented. The active FDI framework is applied to the RBS module in Section V to estimate the minimal detectable fault amplitude and to analyze the fault isolation properties. The experimental validation is performed using two emulated faults. Finally, Section VI concludes this article.

II. Electrical Model of the Reconfigurable Battery Module

In this article, the model of a reconfigurable battery cell as presented in [28] is used. Fig. 1 shows the electrical model of one single cell and Fig. 2 shows the interconnection of six cells in a 2s3p configuration. The cells 1, 2, and 3 connected in parallel are referred as the first row, whereas cells 4, 5, and 6 as the second row. The dynamic of the cell model with the input current i_{cell} and the output voltage v_{cell} is written as [29]

$$\begin{bmatrix} \dot{\text{SoC}} \\ \dot{v_{\text{p}}} \end{bmatrix} = \begin{bmatrix} 0 & 0 \\ 0 & -\tau_{\text{p}}^{-1} \end{bmatrix} \cdot \begin{bmatrix} \text{SoC} \\ v_{\text{p}} \end{bmatrix} + \begin{bmatrix} Q^{-1} \\ C_{\text{p}}^{-1} \end{bmatrix} \cdot i_{\text{cell}} \tag{1}$$

$$\begin{bmatrix} v_{\text{cell}} \end{bmatrix} = \begin{bmatrix} E_{\text{m}}/\,\text{SoC} & 1 \end{bmatrix} \cdot \begin{bmatrix} \text{SoC} \\ v_{\text{p}} \end{bmatrix} + \begin{bmatrix} R_{\text{o}} \end{bmatrix} \cdot i_{\text{cell}} \tag{2}$$

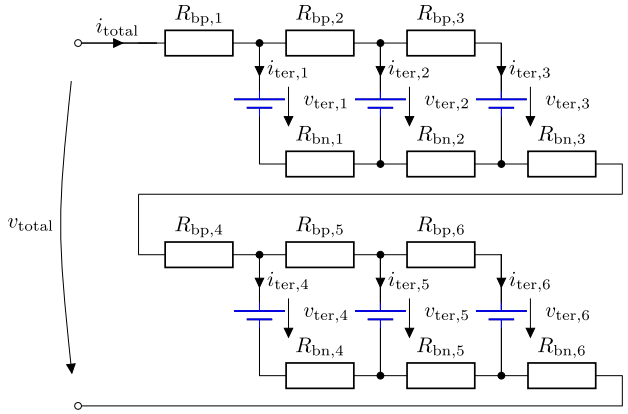

Fig. 2. Electrical connection of six RBS cells (blue, see Fig. 1) taking into account the busbar resistances $R_{\text{bp},i}$, $R_{\text{bn},i}$. The first row contains cells 1, 2, and 3; the second row contains cells 4, 5, and 6 (2s3p configuration).

where E_{m} is the open-circuit voltage (electromotive force), SoC the state of charge, and v_{p} the polarization voltage of the resistor–capacitance-element (*RC*-element). Q denotes the capacity of the cell and $\tau_{\text{p}} = R_{\text{p}}C_{\text{p}}$ the time constant of the *RC*-element. By parameterizing the model according to the cell type used, a wide range of cell types with different capacities can be modeled. Due to the connection of the cell to the busbar, a contact resistance R_{con} arises. The busbar itself is modeled by resistors $R_{\text{bn},i}$ and $R_{\text{bp},i}$. The galvanic cell can be bridged with the BS and connected to the power path with the AS. The switches are modeled as ideal resistors with a very high OFF-resistance $R_{\text{act}} = R_{\text{act,off}}$, $R_{\text{byp}} = R_{\text{byp,off}}$ and a small ON-resistance $R_{\text{act}} = R_{\text{act,on}}$, $R_{\text{byp}} = R_{\text{byp,on}}$. Only one of the two switches may be closed (ON-state) at a time, resulting in the following three switch states: *Active* state, if the AS is closed; *Bypass* state, if the BS is closed; *Idle* state, if neither switch is closed.

Within the scope of FDI, faults are modeled according to $\theta = \theta_0 + f_\theta$ with θ_0 being a fault-free parameter or sensor value and f_θ the respective fault value. The considered faults are

$$\theta \in \{i_{\text{cell},i}, i_{\text{total}}, v_{\text{cell},i}, v_{\text{total}}, E_{\text{m},i}, R_{\text{o},i}, R_{\text{con},i}, R_{\text{bn},i}, R_{\text{bp},i}, R_{\text{act,on},i}, R_{\text{byp,off},i} \mid i \in [1,6]\}. \quad (3)$$

To avoid the excessive use of case distinctions, it is assumed that all cells are initially in the active state. Therefore, only the faults $f_{R_{\text{act,on},i}}$ and $f_{R_{\text{byp,off},i}}$ can occur at the switches. As in [18] and [30], the single-fault assumption and the closed world assumption are made. This means that only one fault can be present at any given time and that the diagnosis framework has full knowledge of all possible faults that could occur in the system.

III. Residual-Based Parameter Estimation

Fig. 3 summarizes the complete framework for active fault diagnosis. In the following, the implemented residuals are presented, which were used for active fault diagnosis. Based on these residuals, a constrained parameter estimator is applied to calibrate the system during the fault-free operation.

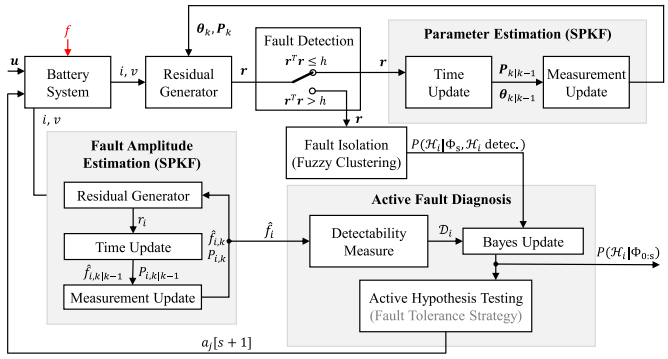

Fig. 3. Framework for active model-based fault diagnosis.

A. Implemented Residuals

The ten smallest MSO subsystems for all faults in the system are calculated using an algorithm for finding MSO subsystems [31]. Based on the resulting MSO sets one residual for each fault is implemented. The smallest MSO subsystem containing the faults $f_{R_{\text{con},i}}$ and $f_{R_{\text{act,on},i}}$ is a Kirchhoff's voltage law (KVL) loop with the next cell. The second smallest set is a KVL loop with the nonadjacent cell, whereas the cell in between is in *Idle* state. Residuals for both MSO sets are implemented to enhance the isolability through active fault diagnosis. The smallest MSO subsystem containing $f_{R_{\text{o},i}}$ consists of the equations that describe the dynamic behavior of the cell. This is implemented using an adaptive Kalman filter. Hereby, the expectation–maximization algorithm by Bavdekar *et al.* [32] is used to identify the process and measurement noise of the Kalman filter. The faults $f_{E_{\text{m},i}}$ and $f_{v_{\text{cell},i}}$ are evaluated by opening the AS of the respective cell, so that the external excitation of the Li-ion cell can be neglected. Faults in the current sensors $f_{i_{\text{cell},i}}$ are evaluated by opening the AS. Then, it follows $i_{\text{cell},i} \approx 0$. The smallest MSO set for $f_{i_{\text{total}}}$ and faults in $R_{\text{byp,off}}$ are based on Kirchhoff's current law for each row in the battery system $i_{\text{total}} = \sum_{k=1}^{n_{\text{par}}} i_{\text{cell},k}$. A fault in the total voltage sensor $f_{v_{\text{total}}}$ and faults in busbar resistances $R_{\text{bp},i}, i \in \{1,4\}$ and $R_{\text{bn},i}, i \in \{3,6\}$ are best diagnosed by a KVL loop over the whole module while all cells are in the *Active* state.

Inspired by Gustafsson [33], a normalized residual space is used. Therefore, the residuals are assumed to be Gaussian distributed with a known variance $\boldsymbol{\Sigma}_{\tilde{r}}$. This requires Gaussian distributed process and measurement noise, as also often assumed in literature [34]–[38]. The normalized residual space is then a linear transformation

$$\boldsymbol{r} = \boldsymbol{L}^T \tilde{\boldsymbol{r}} \quad (4)$$

with $\boldsymbol{L} = (\text{chol}(\boldsymbol{\Sigma}_{\tilde{r}}))^{-1}$, the residual vector $\tilde{\boldsymbol{r}}$, and the Cholesky decomposition $\text{chol}(\cdot)$. The resulting normalized residuals $\boldsymbol{r} \in \mathbb{R}^n$ are independent normally distributed. This simplifies fault detection and enhances fault sensitivity.

B. Constrained Parameter Estimator

Model uncertainties can deteriorate the performance of a model-based FDI approach [39]. In this article, a parameter

Algorithm 1: An SVD Based Approach for SPKF [42], [43].

System

$$\boldsymbol{\theta}_k = \boldsymbol{\theta}_{k-1} + \boldsymbol{\omega}_{k-1} \qquad \boldsymbol{\omega} \sim \mathcal{N}(\mathbf{0}, \boldsymbol{\Sigma}_{\boldsymbol{\omega},k}) \quad 1$$

$$\mathbf{d}_k = \mathbf{r}(\mathbf{x}_k, \mathbf{u}_k, \boldsymbol{\theta}_k) + \boldsymbol{\nu}_k \qquad \boldsymbol{\nu}_k \sim \mathcal{N}(\mathbf{0}, \mathbf{I}) \quad 2$$

Constraints

$$\widehat{\boldsymbol{\theta}}_k > \mathbf{0} \quad 3$$

$$\widehat{\boldsymbol{\theta}}_k \approx \widehat{\boldsymbol{\theta}}_0 + \boldsymbol{\xi}_\theta \qquad \boldsymbol{\xi}_\theta \sim \mathcal{N}(\mathbf{0}, \boldsymbol{\Sigma}_\xi) \quad 4$$

Definitions

$$L = \dim(\boldsymbol{\theta}_k) \quad 5$$

$$\gamma: \quad 1 \le \gamma \le \sqrt{2} \quad 6$$

$$\alpha_i^{(m)} = \tfrac{1}{2L} \qquad 1 \le i \le L \quad 7$$

$$\alpha_0^{(c)} = \tfrac{\kappa}{L+\kappa} \quad 8$$

$$\alpha_i^{(c)} = \tfrac{1}{2L+2\kappa} \qquad 1 \le i \le L \quad 9$$

Initialization

$$\widehat{\boldsymbol{\theta}}_0 = E[\boldsymbol{\theta}_0] \quad 10$$

$$\widehat{\mathbf{P}}_0 = E[(\boldsymbol{\theta}_0 - \widehat{\boldsymbol{\theta}_0})(\boldsymbol{\theta}_0 - \widehat{\boldsymbol{\theta}_0})^T] \quad 11$$

Loop: for $k \in \{1, 2, ..., \infty\}$

Time update and sigma point calculation

$$\widehat{\boldsymbol{\theta}}_k^- = \widehat{\boldsymbol{\theta}}_{k-1} \quad 12$$

$$\mathbf{P}_{k|k-1} = \mathbf{P}_{k-1} + \boldsymbol{\Sigma}_{\boldsymbol{\omega},k-1} \quad 13$$

$$[\mathbf{U}, \mathbf{S}, \mathbf{V}] = \mathrm{SVD}(\mathbf{P}_{k-1}) \quad 14$$

$$\mathbf{W}_{k|k-1} = \left[\widehat{\boldsymbol{\theta}}_k^- \quad \widehat{\boldsymbol{\theta}}_k^- + \gamma\mathbf{U}\sqrt{\mathbf{S}} \quad \widehat{\boldsymbol{\theta}}_k^- - \gamma\mathbf{U}\sqrt{\mathbf{S}}\right] \quad 15$$

$$\mathbf{D}_{k|k-1} = \begin{bmatrix} \mathbf{r}(\mathbf{x}_k, \mathbf{u}_k, \mathbf{W}_{k|k-1}) \\ \frac{\mathbf{W}_{k|k-1} - \boldsymbol{\theta}_0}{\boldsymbol{\theta}_0} \end{bmatrix} \quad 16$$

$$\widehat{\mathbf{d}}_k = \mathbf{D}_{k|k-1,0} + \sum_{i=1}^{2L} \alpha_i^{(m)} \mathbf{D}_{k|k-1,i} \quad 17$$

Measurement update

$$\mathbf{P}_{\widehat{d}_k,\widehat{d}_k} = \sum_{i=0}^{2L} \alpha_i^{(c)} (\mathbf{D}_{k|k-1,i} - \widehat{\mathbf{d}}_k)(\mathbf{D}_{k|k-1,i} - \widehat{\mathbf{d}}_k)^T + \begin{bmatrix} \mathbf{I} \\ \boldsymbol{\Sigma}_\xi \end{bmatrix} \quad 18$$

$$\mathbf{P}_{\widehat{\theta}_k,\widehat{d}_k} = \sum_{i=0}^{2L} \alpha_i^{(c)} (\mathbf{W}_{i,k|k-1} - \widehat{\boldsymbol{\theta}}_k^-)(\mathbf{D}_{i,k|k-1} - \widehat{d}_k)^T \quad 19$$

$$\mathbf{K}_k = \mathbf{P}_{\widehat{\theta}_k,\widehat{d}_k} \mathbf{P}^{-1}_{\widehat{d}_k,\widehat{d}_k} \quad 20$$

$$\widehat{\boldsymbol{\theta}}_k = \widehat{\boldsymbol{\theta}}_k^- + \mathbf{K}_k(\mathbf{0} - \widehat{\mathbf{d}}_k) \quad 21$$

$$\widehat{\boldsymbol{\theta}}_k(\widehat{\boldsymbol{\theta}}_k < 0) = \widehat{\boldsymbol{\theta}}_0(\widehat{\boldsymbol{\theta}}_k < 0) \quad 22$$

$$\mathbf{P}_k = \mathbf{P}_{k|k-1} - \mathbf{K}_k \mathbf{P}_{\widehat{d}_k,\widehat{d}_k} \mathbf{K}_k^T \quad 23$$

estimator is used for system calibration in order to decrease the model uncertainties. Due to the nonlinearities in the considered system, a sigma-point Kalman filter (SPKF) is implemented. In the literature, a common choice for SPKF implementation is the square-root SPKF by van der Merwe and Wan [40], which is also used by Plett [41] for Li-ion cells. For the present application, however, the square-root SPKF runs into numerical problems. Therefore, the SPKF based on the singular value decomposition (SVD) as proposed by Chen [42] is used for parameter estimation (Algorithm 1). The SVD implementation proves to be stable for the considered system, however its computational complexity is $\mathcal{O}(N^3)$ [42] as compared to $\mathcal{O}(N^2)$ for the square-root SPKF [41]. The aim of the SVD-based SPKF is to drive the fault-free residual values to zero, as shown in Algorithm 1, line 21. In order to increase the numerical stability, the estimated parameters are normalized

$$\widehat{\boldsymbol{\theta}}_k \approx \widehat{\boldsymbol{\theta}}_0 = \mathbf{1}. \quad (5)$$

Each cell $i \in [1, 6]$ in the battery system is modeled with different parameters ($j \in [1, 24]$)

$$\mathrm{CP}_j \in \{E_{\mathrm{m},i}, R_{\mathrm{o},i}, C_{\mathrm{p},i}, R_{\mathrm{p},i} \mid i \in [1, 6]\} \quad (6)$$

to account for manufacturing tolerances. Furthermore, an SoC model $\overline{\mathrm{CP}}_j(\mathrm{SoC})$ for each cell parameter is used

$$\widehat{\mathrm{CP}}_{k,j} = \underbrace{\widehat{\theta}_{k,j}}_{\approx 1} \cdot \overline{\mathrm{CP}}_j(\mathrm{SoC}). \quad (7)$$

Also, the system parameters ($j \in [1, 30]$)

$$\mathrm{SP}_j \in \{R_{\mathrm{con},i}, R_{\mathrm{bn},i}, R_{\mathrm{bp},i}, R_{\mathrm{act,on},i}, R_{\mathrm{byp,off},i} \mid i \in [1, 6]\} \quad (8)$$

outside the galvanic cell, such as the contact and the busbar resistances as well as the resistances of the switches, are affected by uncertainties. Since there are far more parameters to estimate than measurements are available, a constrained approach is used for parameter estimation. Hereby, two constraints for each parameter are used

$$\widehat{\boldsymbol{\theta}}_k \approx \widehat{\boldsymbol{\theta}}_0 + \boldsymbol{\xi}_\theta \qquad \boldsymbol{\xi}_\theta \sim \mathcal{N}(\mathbf{0}, \boldsymbol{\Sigma}_\xi) \quad (9a)$$

$$\widehat{\boldsymbol{\theta}}_k > \mathbf{0}. \quad (9b)$$

Each parameter is forced by (9a) to remain in the region of the start value $\widehat{\boldsymbol{\theta}}_0$, representing the parameter of the average cell. The size of the region is adjusted with the matrix $\boldsymbol{\Sigma}_\xi$. As proposed by Simon [44], (9a) is added as an additional measurement to the parameter estimator in Algorithm 1, line 16: The residuals and the normalized deviation from the start value are calculated for the sigma-points $\mathbf{W_{k|k-1}}$. This constraint represents the previous knowledge on the system parameters. For FDI purposes, the system is generally well known, only manufacturing tolerances need to be compensated. The average cell parameters are identified in the laboratory through cell characterization tests. The parameters of the electronics on the printed circuit board (PCB) are also measurable. Thus, average values for most system parameters are known. Only the contact resistances $R_{\mathrm{c},i}$ of each cell are impracticable to measure, since they change with each test setup. Therefore, constraint (9a) is omitted for $R_{\mathrm{con},i}$. Constraint (9b) is motivated by the physical properties of the parameters, since, for example, resistor values should not become negative. In Algorithm 1, line 22 the constraint (9b) is added similar to the estimate projection in [44] and [45]. As soon as a parameter estimate $\widehat{\theta}_{k,j}$ drops below zero, it is set to its start parameter $\widehat{\theta}_{0,j}$. This procedure gives the parameter estimator time to readjust all the parameters such that $\widehat{\theta}_{k,j} \ge 0$.

For the present system, $\boldsymbol{\Sigma}_\xi$ is chosen as a diagonal matrix with

$$\mathrm{diag}(\boldsymbol{\Sigma}_\xi) = \begin{cases} 30 & \forall\ \mathrm{SP}_j, \mathrm{CP}_j \ne R_{\mathrm{act,on},i} \\ 1 & \forall\ R_{\mathrm{act,on},i}. \end{cases} \quad (10)$$

A smaller value on the diagonal of $\boldsymbol{\Sigma}_\xi$ is selected for the parameter $R_{\mathrm{act,on},i}$ as unlike contact resistances, the value remains

largely constant and is measurable on the PCB. The process variance $\mathbf{\Sigma}_{\boldsymbol{\omega},k}$ is also a diagonal matrix with

$$\operatorname{diag}(\mathbf{\Sigma}_{\boldsymbol{\omega},k}) = \begin{cases} 5\cdot 10^{-13} & \forall\ \mathrm{SP}_j, \mathrm{CP}_j \neq E_{\mathrm{m},i} \\ 5\cdot 10^{-15} & \forall\ E_{\mathrm{m},i}. \end{cases} \tag{11}$$

The start parameter variance $\widehat{\boldsymbol{P}}_0$ is set to

$$\operatorname{diag}(\widehat{\boldsymbol{P}}_0) = \begin{cases} 5\cdot 10^{-5} & \forall\ \mathrm{SP}_j, \mathrm{CP}_j \neq E_{\mathrm{m},i} \\ 5\cdot 10^{-7} & \forall\ E_{\mathrm{m},i}. \end{cases} \tag{12}$$

For the considered application γ is set to $\gamma = \sqrt{2}$ and $\kappa = 3 - L$. The number of parameters L in the 2s3p system is $L = 54$.

IV. Fault Diagnosis

The passive fault isolation is done by a fuzzy clustering approach. To increase robustness, a detectability measure is introduced for cases where faults are structurally but not analytically detectable. To enable active fault isolation, the policy π_2 by [25] is adjusted in such a way that no kernel estimation for the next action is required.

A. Passive FDI

The χ^2-test is used for fault detection. In the following the i-th residual at time k is denoted as $r_i[k]$. According to (4), $r_i[k]$ is approximately independent normal distributed; therefore, the squared sum

$$g_{M,i}[k] = \sum_{j=k-M+1}^{k} r_i^2[j] \tag{13}$$

of $r_i[k]$ over a time window with the length M approximately follows the χ^2-distribution with M degrees of freedom

$$g_{M,i}[k] \sim \chi^2_M. \tag{14}$$

A greater M leads to a higher detection delay, but offers better sensitivity [39]. The value $M = 30$ offers a good sensitivity and a low detection delay for the present system. For a given false alarm probability α, a threshold h for $g_{M,i}[k]$ is calculated based on the PDF $\rho_{\chi^2_M}(x)$ of the χ^2_M-distribution as [39]

$$\int_h^\infty \rho_{\chi^2_M}(x)\,\mathrm{d}x = \alpha. \tag{15}$$

Fault isolation is done with a fuzzification of the diagnosis algorithm proposed by Gustafsson [33]. After fault detection, the direction of the residual vector for each fault is calculated and compared to the current residual vector. The diagnosed fault is the fault that minimizes the angle between its direction and the current residual. According to Gustafsson [33], the ith fault at time k is isolated by $\widehat{i}[k] = \arg\min_i d_i[k]$, with

$$d_i[k] = \left\| \frac{\boldsymbol{r}[k]}{\|\boldsymbol{r}[k]\|} - \frac{\boldsymbol{\mu}_i}{\|\boldsymbol{\mu}_i\|} \right\|^2 = \operatorname{angle}\left(\boldsymbol{r}[k], \boldsymbol{\mu}_i\right). \tag{16}$$

Here, $\boldsymbol{\mu}_i$ denotes the direction the residual vector would take in case the ith fault has occurred. Note that the positive and negative fault amplitudes have to be treated separately, as the direction-vector $\boldsymbol{\mu}_i$ for the opposite sign points in the opposite direction [33]. In order to include a confidence about the decision, the fault isolation approach is fuzzyfied. For each point in time, a membership degree $u_i[k] \in [0,1]$ with $\sum_{j=1}^{C} u_j[k] = 1$ for each fault is calculated based on the current residual vector $\mathbf{r}[k]$ as [46], [47]

$$u_i[k] = \begin{cases} \left(\sum_{j=1}^{C} \left(\frac{d_i[k]}{d_j[k]} \right)^{2/(l-1)} \right)^{-1} & d_i[k] \neq 0 \\ 1 & d_i[k] = 0 \end{cases} \tag{17}$$

with $l > 1$ and C being the total number of faults. The fuzzification also allows diagnosing parameter and sensor faults in a joined framework. By collecting N residual samples and assuming detectability, the probability for each fault, hypothesis $\mathcal{H}_i \in \mathbb{H}$, is calculated as

$$P(\mathcal{H}_i|\Phi_s, \mathcal{H}_i \text{ detec.}) = \left(1 - \tilde{P}(\mathcal{H}_0|\Phi_s)\right) \frac{1}{N} \sum_{k=1}^{N} u_i[k] \tag{18}$$

with the probability of no fault $\tilde{P}(\mathcal{H}_0|\Phi_s)$. Similar to the notation in [30], Φ_s is the observation space during the switch state s, and $\mathbb{H}$ is the set of hypotheses. The ith fault has to be structurally detectable.

Next, the probability of no fault $\tilde{P}(\mathcal{H}_0|\Phi_s)$ is calculated. Consider the squared norm of a residual vector $||\mathbf{r}||^2 = ||\mathbf{d} + \mathbf{f}||^2$ at any time k with the noise vector $\mathbf{d} \sim \mathcal{N}(\mathbf{0}, \mathbf{I})$ and the unknown influence of the fault $\mathbf{f} \in \mathbb{R}^n$. Hence, the norm $||\mathbf{r}||^2$ is distributed according to a noncentered $\chi^2_{n,\lambda}$ distribution with the displacement parameter

$$\lambda = \sum_{i=1}^{n} f_i^2 \tag{19}$$

and n degrees of freedom. The expected value of $||\mathbf{r}||^2$ is calculated as

$$\begin{aligned} E\left[||\mathbf{r}||^2\right] &= E\left[\sum_{j=1}^{n} \left(d_j^2 + f_j^2 + 2 d_j f_j\right)\right] \\ &= \sum_{j=1}^{n} \left(\underbrace{E\left[d_j^2\right]}_{=1} + E\left[f_j^2\right] + 2\underbrace{E\left[d_j f_j\right]}_{=0} \right) \\ &= n + \sum_{j=1}^{n} f_j^2. \end{aligned} \tag{20}$$

Under the assumption of constant fault portion $\mathbf{f}[k] \approx \text{const.}$, the probability of no fault is approximated by the area between the noncentered $\chi^2_{n,\lambda}$ and the centered χ^2_n-distribution with n degrees of freedom and $\lambda = \operatorname{mean}_k(\|\boldsymbol{r}[k]\|) - n$

$$\begin{aligned} \tilde{P}(\mathcal{H}_0|\Phi_s) &= \int_0^\infty \min\left(\rho_{\chi^2_n}(x), \rho_{\chi^2_{n,\lambda}}(x)\right) \mathrm{d}x \\ &= 1 - F_{\chi^2_n}(\widehat{x}) + F_{\chi^2_{n,\lambda}}(\widehat{x}). \end{aligned} \tag{21}$$

Here, $\widehat{x}$ denotes the intersection of the centered and the noncentered $\chi^2_{n,\lambda}$-distribution (see Fig. 4).

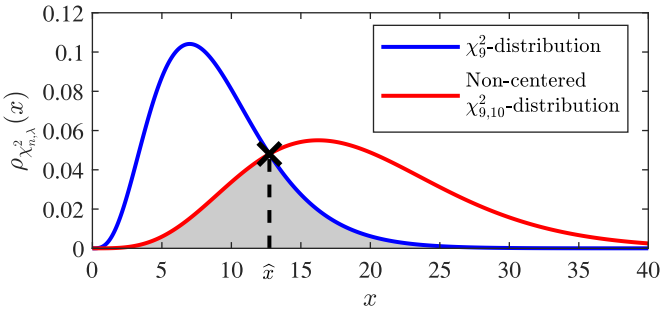

Fig. 4. Distribution of the squared residual vector norm in the fault-free case (blue) and the faulty case (red). The gray marked area below both distributions indicates the probability of no fault $\tilde{P}(\mathcal{H}_0|\Phi_s)$.

B. Detectability Measure

The prerequisite for the hypothesis declaration is the analytical detectability of faults. Consider the case where fault f_1 and f_2 are equiprobable after detection. Assume the FDI algorithm chooses a switch state, in the following called *action* $a_j \in \mathbb{A}$, where f_1 is still structurally detectable, but f_2 is not. If the residuals are approximately zero after a_j, the algorithm could incorrectly conclude that fault f_2 is present since $\boldsymbol{r} \approx 0$ indicates a fault-free system. However, this can be the wrong decision if f_1 is structurally but not analytically detectable after action a_j.

The detectability of a fault is quantified with the sensitivity of residuals toward the fault and an estimation of the fault amplitude. If the fault amplitude is not available, the minimal detectable fault amplitude (see Section V-A) is used, resulting in a maximal conservative decision. Within the FDI framework however, the fault amplitude for each fault is estimated by a separate SPKF (see Section III-B) with the fault model $f_i[k] = f_i[k-1] + \xi_{f_i}$ and $\xi_{f_i} \sim \mathcal{N}(0, \sigma^2_{f_i})$. Considering a linear residual vector

$$\mathbf{r}[k] = \mathbf{H}_d[k]\mathbf{d} + \mathbf{H}_f[k]\mathbf{f} \tag{22}$$

with the disturbances $\mathbf{d}$ and the faults $\mathbf{f}$, the sensitivity of the residual is given as follows [48]:

$$S_f = ||\mathbf{H}_f[k]||. \tag{23}$$

According to Ding [48], this represents the best-case scenario of the influence of $\mathbf{f}$. For faults that do not affect the residuals linearly as in (22), the sensitivity is approximated by the derivative evaluated at the operating point OP

$$S_f = \left|\left| \left.\frac{\delta \mathbf{r}[k]}{\delta \mathbf{f}}\right|_{\text{OP}} \right|\right|. \tag{24}$$

On this basis, the detectability $\mathcal{D}_i$ for fault f_i to be detectable is defined by Definition IV.1.

Definition IV.1: Detectability (quantified) Let $\mathbf{r}$ be a n-dimensional residual vector and S_i be the sensitivity of $\mathbf{r}$ to the ith fault. Furthermore, let the fault amplitude be known as f_i. The detectability is quantified as

$$\begin{aligned}\mathcal{D}_i &= 1 - \int_0^\infty \min\left(\rho_{\chi^2_n}(x),\, \rho_{\chi^2_{n,\lambda}}(x)\right) \mathrm{d}x \\ &= F_{\chi^2_n}(\widehat{x}) - F_{\chi^2_{n,\lambda}}(\widehat{x})\end{aligned} \tag{25}$$

with

$$\lambda = S_i^2 f_i^2 \tag{26}$$

where $\rho_{\chi^2_{n,\lambda}}(x)$ represents the PDF of the noncentral χ^2-distribution with n degrees of freedom and the offset λ, $F_{\chi^2_{n,\lambda}}(x)$ the cumulative PDF, and $\widehat{x} \in \{x \in \mathbb{R} \mid \rho_{\chi^2_n}(x) = \rho_{\chi^2_{n,\lambda}}(x), \lambda = S_i^2 f_i^2\}$ (see Fig. 4).

Note the similarities to the calculation of the probability for $\mathcal{H}_0$ as in (21). $\mathcal{D}_i$ given by Definition IV.1 is seen as the probability for the fault f_i to be detectable in the current measurement space $P(\mathcal{H}_i \text{ detec.}|\Phi_s)$. Assuming the fault f_i becomes undetectable after action a_j, the hypothesis $\mathcal{H}_i$ becomes equal to $\mathcal{H}_0$. In order to still be able to quantify the probability for $\mathcal{H}_i$, the following formula based on (21) is proposed:

$$P(\mathcal{H}_i|\Phi_s, \mathcal{H}_i \text{ not detec.}) = \frac{\widehat{P}_i}{\sum_{j=0}^{|\mathbb{H}|}(1-\mathcal{D}_j)\widehat{P}_j}\tilde{P}(\mathcal{H}_0|\Phi_s) \tag{27}$$

with $|\mathbb{H}|$ being the cardinality of the set of hypotheses and $\widehat{P}_i$ defined in (37). Therefore, the probability for each fault under measurement space Φ_s is given as

$$\begin{aligned}P(\mathcal{H}_i|\Phi_s) = \mathcal{D}_i P(\mathcal{H}_i|\Phi_s, \mathcal{H}_i \text{ detec.}) \\ + (1-\mathcal{D}_i)P(\mathcal{H}_i|\Phi_s, \mathcal{H}_i \text{ not detec.})\end{aligned} \tag{28}$$

using (18), (25), and (27). Note that for $k = 0$, $P(\mathcal{H}_i|\Phi_0)$ is not defined. However, by definition the fault responsible for the detection has to be detectable for $s = 0$, thus

$$P(\mathcal{H}_i|\Phi_0) = \begin{cases} P(\mathcal{H}_i|\Phi_0, \mathcal{H}_i \text{ detec.}) & i \neq 0, \mathcal{H}_i \text{ struc. detec.} \\ \tilde{P}(\mathcal{H}_0|\Phi_0) & i = 0 \\ 0 & \text{otherwise.} \end{cases} \tag{29}$$

C. Active Fault Isolation

The idea of active fault isolation in RBS is to open and close switches in order to improve the confidence in each fault and enhance the isolation possibilities. The confidence in each fault is updated using recursive Bayesian estimation and Bayes' theorem [42], [49]

$$\begin{aligned}P\left(\mathcal{H}_i \,|\mathbf{\Phi}_{0:s}\right) &= \frac{P(\Phi_s \mid \mathcal{H}_i) P\left(\mathcal{H}_i \,|\mathbf{\Phi}_{0:s-1}\right)}{P\left(\Phi_s \,|\mathbf{\Phi}_{0:s-1}\right)} \\ &= \frac{P\left(\mathcal{H}_i \,|\Phi_s\right) P\left(\mathcal{H}_i\right) P\left(\mathcal{H}_i \,|\mathbf{\Phi}_{0:s-1}\right)}{P\left(\Phi_s\right) P\left(\Phi_s \,|\mathbf{\Phi}_{0:s-1}\right)}\end{aligned} \tag{30}$$

with

$$\mathbf{\Phi}_{0:s} = \bigcap_{\zeta=0}^{s} \Phi_\zeta. \tag{31}$$

The denominator does not need to be known since

$$\sum_{i=1}^{|\mathbb{H}|} P\left(\mathcal{H}_i \,|\mathbf{\Phi}_{0:s}\right) = 1 \;\forall s \tag{32}$$

holds (closed world assumption). $P(\mathcal{H}_i \mid \Phi_s)$ is calculated according to (28) and (29). $P(\mathcal{H}_i)$ is a prior that needs to be

set beforehand. According to Isermann [50], the importance of the priors should not be underestimated. A careful selection improves the FDI performance. If, however, no knowledge on $P(\mathcal{H}_i)$ is available, they are commonly set to $P(\mathcal{H}_i) = 1/|\mathbb{H}|$. This choice is also made in this article and leads to very good isolation results, as shown in Section V-B.

Next, the policy to choose the subsequent action $a_j[s+1]$ is introduced. The number of possible actions to be taken is denoted as J. Since sequential and adaptive testing outperform nonsequential and nonadaptive solutions [26], an adaptive, sequential approach is chosen. The aim of active sequential hypothesis testing is to find sensing actions

$$\boldsymbol{A}_{0:S} = \bigcap_{s=0}^{S} a_j[s] \tag{33}$$

a stopping state S and a declaration rule $d : \boldsymbol{\Phi}_{0:S} \times \boldsymbol{A}_{0:S} \to \mathbb{H}$, such that the expected total cost minimizes. The observation space Φ_s may consist of residuals or measurements. The expected total cost γ_{ETC} is written as

$$\gamma_{\mathrm{ETC}} = E[S] + L\mathrm{Pe} \tag{34}$$

with the cost L of making a wrong declaration

$$\mathrm{Pe} = P\left(d\left(\boldsymbol{\Phi}_{0:S-1}, \boldsymbol{A}_{0:S-1}\right) \neq \mathcal{H}_i\right) \tag{35}$$

denotes the probability of making the wrong declaration, i.e., not declaring $\mathcal{H}_i$, even though $\mathcal{H}_i$ is true. $E[S]$ is the expected number of actions that need to be taken until $\mathcal{H}_i$ is accepted. $a_j[s+1]$ denotes a possible next action after $a_j[s]$. In the following, the second policy π_2 by Naghshvar and Javidi [25] is adapted to be independent on the fault amplitude estimation. The adaption increases robustness against false fault amplitude estimation. The policy chooses from J possible actions the next action $a_j[s+1]$ that promises the highest information gain in its confidence in the hypotheses. In [25], the kernel $\rho_i^{(a_j[s+1])}$ for hypothesis $\mathcal{H}_i = \text{true}$ after action $a_j[s+1]$ is compared to the expected PDF $\overline{\rho}_i^{(a_j[s+1])}$ of the residuals for $\mathcal{H}_i = \text{false}$. Hereby, $\overline{\rho}_i^{(a_j[s+1])}$ is calculated as

$$\overline{\rho}_i^{(a_j[s+1])} = \sum_{j \neq i} \frac{\widehat{P}_j}{1 - \widehat{P}_i} \rho_j^{(a_j[s+1])} \tag{36}$$

with

$$\widehat{P}_i := P\left(\mathcal{H}_i \,|\boldsymbol{\Phi}_{0:s}\right). \tag{37}$$

In this article however, the residual direction $\boldsymbol{\mu}_i^{(a_j[s+1])}$ for each next possible action $a_j[s+1]$ in case $\mathcal{H}_i = \text{true}$ is compared to the residual vector $\overline{\boldsymbol{\mu}}_i^{(a_j[s+1])}$ if $\mathcal{H}_i = \text{false}$. Hereby, we define that if the ith fault (hypothesis $\mathcal{H}_i$) is not structurally detectable after action $a_j[s+1]$, the residual vector $\boldsymbol{\mu}_i^{(a_j[s+1])}$ takes the value $\boldsymbol{\mu}_i^{(a_j[s+1])} = \mathbf{0}$. If $\mathcal{H}_i$ is structurally detectable, then the vector is normalized such that $\|\boldsymbol{\mu}_i^{(a_j[s+1])}\| = 1$. The bigger the difference between these two vectors, the better the expected distinguishability of $\mathcal{H}_i = \text{true}$ to $\mathcal{H}_i = \text{false}$ is. In order to formally describe the policy, the matrix $\boldsymbol{\Lambda} \in \mathbb{R}^{|\mathbb{H}| \times J}$ is introduced.

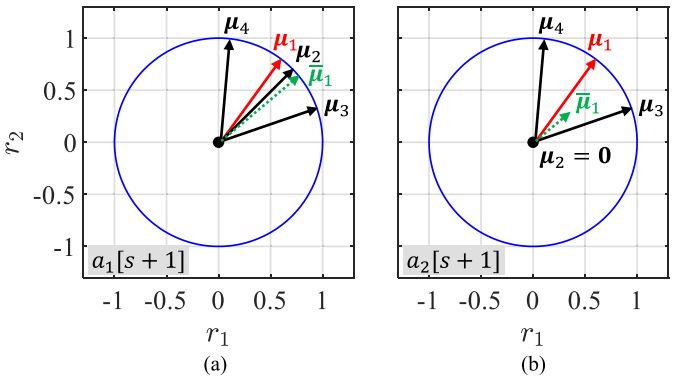

Fig. 5. Figures for Example IV.1: Residual directions for each fault after action $a_1[s+1]$ and after action $a_2[s+1]$ with $\boldsymbol{\mu}_1 : \hat{P}_1 = 0.4$, $\boldsymbol{\mu}_2 : \hat{P}_2 = 0.3$, $\boldsymbol{\mu}_3 : \hat{P}_3 = 0.2$, $\boldsymbol{\mu}_4 : \hat{P}_4 = 0.1$.

The elements of $\boldsymbol{\Lambda}$ are given according to

$$\boldsymbol{\Lambda}_{(i,j)} = \lambda_{a_j} \left|\left| \boldsymbol{\mu}_i^{(a_j)} - \overline{\boldsymbol{\mu}}_i^{(a_j)} \right|\right| \tag{38}$$

with

$$\overline{\boldsymbol{\mu}}_i^{(a)} = \sum_{j \neq i} \frac{\widehat{P}_j}{1 - \widehat{P}_i} \boldsymbol{\mu}_j^{(a)}. \tag{39}$$

The resulting policy is as follows:

1) $\widehat{P}_i < \tilde{p}$: Choose a_j as $\arg\max_{a_j \in \mathbb{A}} \min_{\mathcal{H}_i \in \mathbb{H}} \boldsymbol{\Lambda}$;
2) $\exists \widehat{P}_i \in [\tilde{p}, 1 - L^{-1})$: Choose a_j as $\arg\max_{a_j \in \mathbb{A}} \boldsymbol{\Lambda}_{(i,1:J)}$;
3) If $\exists \widehat{P}_i \geq 1 - L^{-1}$: Retire and accept $\mathcal{H}_i$.

The variable λ_{a_j} is a tuning parameter to prefer some actions to others. In this article, λ_{a_j} is set as $\lambda_{a_j} = \frac{1}{|\mathbb{A}|} \ \forall a_j$. Similarly, $\tilde{p} > 0.5$ is also a tuning parameter and is set to $\tilde{p} = 0.75$.

Example IV.1: Consider the case depicted in Fig. 5. Four hypothesis ($|\mathbb{H}| = 4$) are considered in a two-dimensional residual space $\mathbf{r} \in \mathbb{R}^2$. The probabilities for each hypothesis are $\hat{P}_1 = 0.4$, $\hat{P}_2 = 0.3$, $\hat{P}_3 = 0.2$ and $\hat{P}_4 = 0.1$. Furthermore the residual vectors $\boldsymbol{\mu}_i^{(a_j[s+1])}$ for action $a_1[s+1]$ and $a_2[s+1]$ are shown. f_2 is structurally not detectable in action $a_2[s+1]$, therefore $\boldsymbol{\mu}_2^{(a_2[s+1])} = \mathbf{0}$, depicted as a dot in Fig. 5(b). The vectors $\overline{\boldsymbol{\mu}}_1^{(a_j[s+1])}$ for $j = \{1, 2\}$ are depicted as a dashed line. It is evident that the case $\mathcal{H}_1 = \text{true}$ is far better distinguishable from case $\mathcal{H}_1 = \text{false}$ for $a_2[s+1]$ [Fig. 5(b)] than for $a_1[s+1]$ [Fig. 5(a)].

V. Application to Battery Systems

In the following, the fault isolation properties of the active FDI algorithm (see Fig. 3) are tested simulatively and the minimal detectable fault amplitudes are determined. The constrained parameter estimator and the active FDI algorithm are validated using an experimental setup. It is assumed that contact resistances and the resistances of the busbars and switches increase ($f_i \geq 0$) in the event of a fault. The resistances of open switches and the open-circuit voltage $E_{\mathrm{m},i}$ are assumed to decrease ($f_i \leq 0$) in the event of a fault. No assumption on the fault sign is made for sensor faults and $R_{\mathrm{o},i}$, because sensor faults may have any amplitude and the internal resistance of the cell may

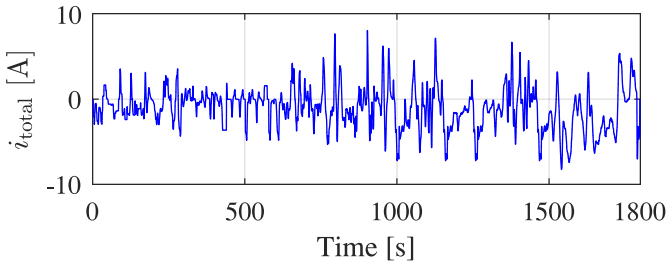

Fig. 6. WLTP-based current profile.

TABLE I
NOISE LEVELS USED FOR THE SIMULATIONS AND THE EXPERIMENTAL VALIDATION

$\sigma^2_{v_{\text{cell},i}}$	$\sigma^2_{i_{\text{cell},i}}$	$\sigma^2_{v_{\text{total}}}$	$\sigma^2_{i_{\text{total}}}$
$1 \cdot 10^{-8}$	$5.8 \cdot 10^{-6}$	$2.6 \cdot 10^{-6}$	$4 \cdot 10^{-4}$

both decrease [(e.g., due to an internal short circuit (ISC)] and increase (e.g., due to aging).

A. Simulative Results

The electrical model of the RBS from Section II is implemented in MATLAB R2019a and excited with a current profile. Similar to [10] and [51], the current profile is based on the 30-min worldwide harmonized light vehicles test procedure (WLTP) [52] and is shown in Fig. 6. The active fault diagnosis is performed using the constrained parameter estimator and the procedure presented in Sections III and IV. The noise levels used for the simulations and the experimental validation are given in Table I. The detection and isolation capacity of the framework is initially tested with a high fault amplitude for each fault in the RBS module of Fig. 2. Sensor faults were tested with an amplitude of ± 1V and ± 1A. Faults in R_{con}, $R_{\text{act,on}}$ and R_{o} were tested with a resistance of $70\,\text{m}\,\Omega$. Faulty busbar resistances R_{bn}, R_{bp} were increased by $10\,\text{m}\,\Omega$. For a fault in the closed BS, its resistance is assumed to decrease to $3.3\,\Omega$. Faults in E_{m} are modeled by a voltage drop of 10%.

The resulting isolability matrix is shown in Fig. 7. The faults denoted on the abscissa are isolated when the faults on the ordinate are introduced. The isolation capability by the passive FDI (see Section IV-A) is marked in black. The further fault isolation through active FDI is shown in grey. Isolability is generally not necessarily a symmetrical property [30]. In our case, the asymmetry is achieved because further knowledge about the sign of the fault is added by the isolation algorithm described in Section IV-A. In this way, a fault in the total voltage sensor v_{total} is isolable from a fault on the busbars in between each row. The additional isolability is achieved by assuming that the resistance on the busbars can only increase and not decrease. Similarly, the faults f_$R_{\text{o},i}$ are isolable from the faults f_$E_{\text{m},i}$, but not the other way around. The improved isolability is achieved by assuming that $E_{\text{m},i}$ can only decrease, whereas $R_{\text{o},i}$ can increase and decrease. By active fault isolation, further isolation is achieved for faults in the contact resistances and faults in the AS. Furthermore, the isolability for the faults f_$E_{\text{m},i}$ and f_$R_{\text{o},i}$ improves. Both faults are isolated symmetrically by the active FDI.

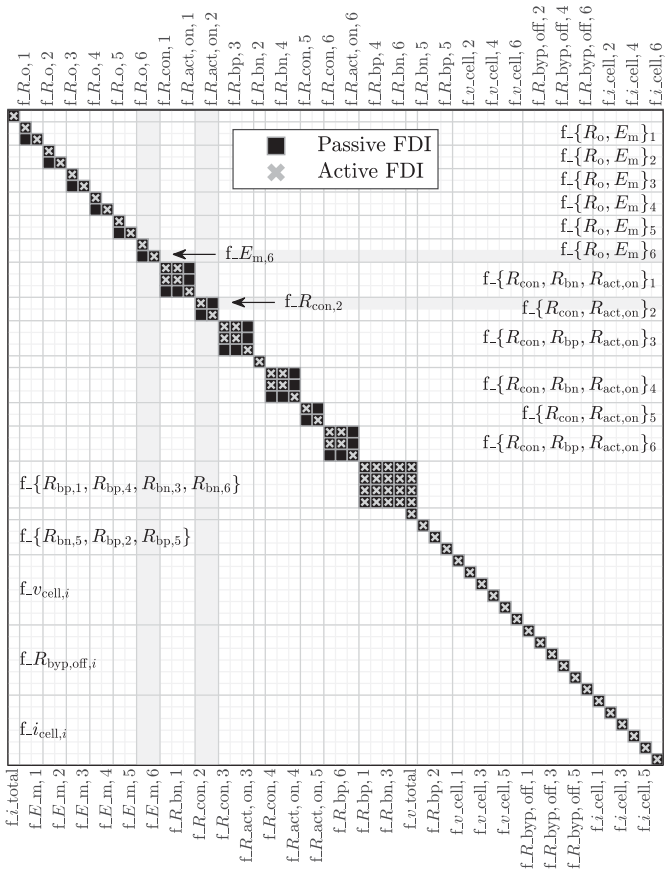

Fig. 7. Fault isolability matrix of the 2s3p battery module. Comparison of passive and active FDI including system knowledge. The labels of the ordinate (introduced fault) and the abscissa (diagnosed fault) are identical. For better readability, the faults of the abscissa are shown on two axes and the faults of the ordinate are summarized by sets and $i = 1 \ldots 6$.

TABLE II
MINIMAL DETECTABLE FAULT AMPLITUDE FOR EVERY FAULT

Index $i =$	1	2	3	4	5	6
$i_{\text{cell},i}$ [mA]	14	15	14	15	16	15
$v_{\text{cell},i}$ [mV]	0.4	0.3	0.4	0.3	0.2	0.4
$E_{\text{m},i}$ [mV]	0.8	1.6	1.6	1.2	0.8	1.6
$R_{\text{o},i}$ [mΩ]	3.1	3.6	4.1	2	2	3.6
$R_{\text{con},i}$ [mΩ]	0.2	0.16	0.24	0.12	0.24	0.2
$R_{\text{bn},i}$ [mΩ]	0.17	0.08	0.53	0.13	0.13	0.53
$R_{\text{bp},i}$ [mΩ]	0.53	0.08	0.24	0.53	0.1	0.2
$R_{\text{act,on},i}$ [mΩ]	0.2	0.16	0.24	0.12	0.24	0.2
$R_{\text{byp,off},i}$ [Ω]	260	260	260	340	320	320
i_{total} : 12 mA, v_{total} : 4.6 mV						

Next, the minimal detectable fault amplitude is found for each fault. The result, shown in Table II, is obtained by subsequently increasing the respective fault within the simulation until it is detected. The FDI algorithm had 400 iterations in order to detect the fault; otherwise, it was counted as a missed detection. The step size of the FDI algorithm is set to $\Delta t = 0.96$s due to the sampling rates of the different sensor systems (10, 40, and 80ms), which are explained later for the experimental setup.

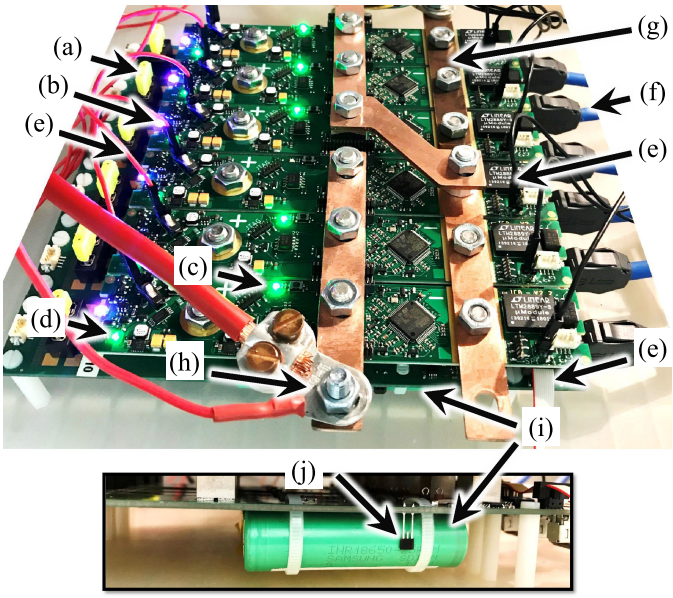

Fig. 8. Experimental setup: The description of the components is given in Table III. A schematic circuit diagram of the experimental setup is drawn in Figs. 1 and 2.

To obtain a realistic prognosis for the minimal detectable fault amplitude, the noise levels of Table I are used. The value of $R_{\mathrm{byp,off},i}$ is the value to which the resistance of the switch has to decrease in order to be detectable. The minimal detectable fault amplitudes vary slightly between the cells. One reason is the different sensitivity of the implemented residuals toward the fault. On the other hand, it is due to the parameter variations of the cell and system parameters. Based on the relatively high noise level of the total current sensor, faults affecting the current sensors are only detected from amplitudes of several milliamperes. The detectability of a fault within the cell ($R_{\mathrm{o},i}$, $E_{\mathrm{m},i}$) does also depend on the sampling rate of the FDI algorithm. The detectability is the same for faults with a negative amplitude.

B. Experimental Results

The proposed active FDI framework is subsequently tested on an experimental setup consisting of six RBS-cells in 2s3p configuration. Based on the implemented residuals, the parameter estimator is used to adapt the model parameters to the real system and estimate the fault amplitude. The validation is based on two emulated faults: The fault $f_{E_{\mathrm{m},6}}$ is emulated by an ISC; the fault $f_{R_{\mathrm{con},2}}$ is emulated by increasing the contact resistance $R_{\mathrm{con},2}$.

1) Experimental Setup: The experimental setup is shown in Fig. 8. A cylindrical Samsung cell (INR18650-25R) with a capacity of $2.5\,\mathrm{A\,h}$ is used for the experiments [see Fig. 8(i)]. Six cells are connected via busbars to form a 2s3p module [see Fig. 8(g)]. All tests are carried out in a temperature chamber at a constant temperature of $25\,^{\circ}\mathrm{C}$. The current excitation is done by a Chroma Module Charge/Discharge Tester. The tester also provides a measurement of the total current and voltage with a time resolution of $40\,\mathrm{ms}$. The signals for fault diagnosis are

TABLE III
DESCRIPTION OF THE EXPERIMENTAL SETUP

(a)	Automotive fuse
(b)	Indicator LED for the state of the board
(c)	Indicator LED for the active switch
(d)	Indicator LED for the external power supply
(e)	External power supply for the PCB
(f)	Connector and cable to the data logger
(g)	Busbars fixed by screw nuts
(h)	Connection of power and sense cable
(i)	Li-ion cell
(j)	Temperature sensor

logged by a PCB connected to the cell terminals with a time resolution of $80\,\mathrm{ms}$. In addition to the sensors, the PCB also contains the two switches. The Li-ion cell itself is soldered to another PCB, which contains a fuse [see Fig. 8(a)] and reference sensors for the voltage, current, and temperature measurement of the cell. The position of the temperature measurement is shown in Fig. 8(j). The logging of the reference sensors is done by a Hioki 8423 data logger with a time resolution of $10\,\mathrm{ms}$ [see Fig. 8(f)]. The PCB is supplied externally with power in order not to influence the measurements [see Fig. 8(e)]. Due to the different sampling times, all measurements are synchronized by time. The reference sensors are solely used for calibration.

2) Learning Process: To learn the parameters of the system the constrained parameter estimator from Section III-B is used. Since the parameters have different learning rates, the first 8 min (fault-free) of each test are repeated until the residuals $\tilde{g}_M$ are below the fault detection threshold $h = 100$. The development of the residuals $\tilde{g}_M$ is shown in Fig. 9(a). From an initial amplitude of $|g_{M,i}| > 1000$, all residuals decrease to an amplitude of $g_{M,i} < h\,\forall i$. From the development of the residuals $\tilde{g}_M$, it can be seen that the estimated parameters describe the system significantly better than the used average values in the beginning. The percentage change $\Delta_\theta = 100 \cdot (\widehat{\theta}_{k,j} - \widehat{\theta}_{0,j})/\widehat{\theta}_{0,j}$ of the corresponding system parameters is shown in Fig. 9(b). The initial parameters are given in Table IV. The open-circuit voltage $E_{\mathrm{m},i}$ is practically unchanged (close to 0%) by the constrained parameter estimator except for spikes at the beginning of the learning process. This is because the SoC was set at the beginning based on the open-circuit voltage (cells were at rest before the measurement started). The development of the system parameters during the learning process shows that the cell resistances ($R_{\mathrm{o},i}$, $R_{\mathrm{p},i}$) in the experimental setup are estimated to be smaller compared to the initial parameters. This is because in the previous characterization of the cells no distinction was made between cell resistance and contacting. The cell resistance is therefore initialized about $2 \cdot R_{\mathrm{con},i}$ too high and corrected by the parameter estimator for the experimental setup of Fig. 8. Furthermore, it is noticeable that a high value for the contact resistance $R_{\mathrm{con},2}$ is already estimated in the fault-free case. To be able to introduce an artificial, faulty contact resistance (see Section V-B4), the screwed contact of the cell with the busbar has to be modified. Thereby, an additional contact resistance in the order of magnitude of $R_{\mathrm{con},2}$ arises (above $f_{R_{\mathrm{con},2}}$ in Fig. 12). Accordingly, the initial, average contact resistance of the fault-free system is estimated by the parameter estimator

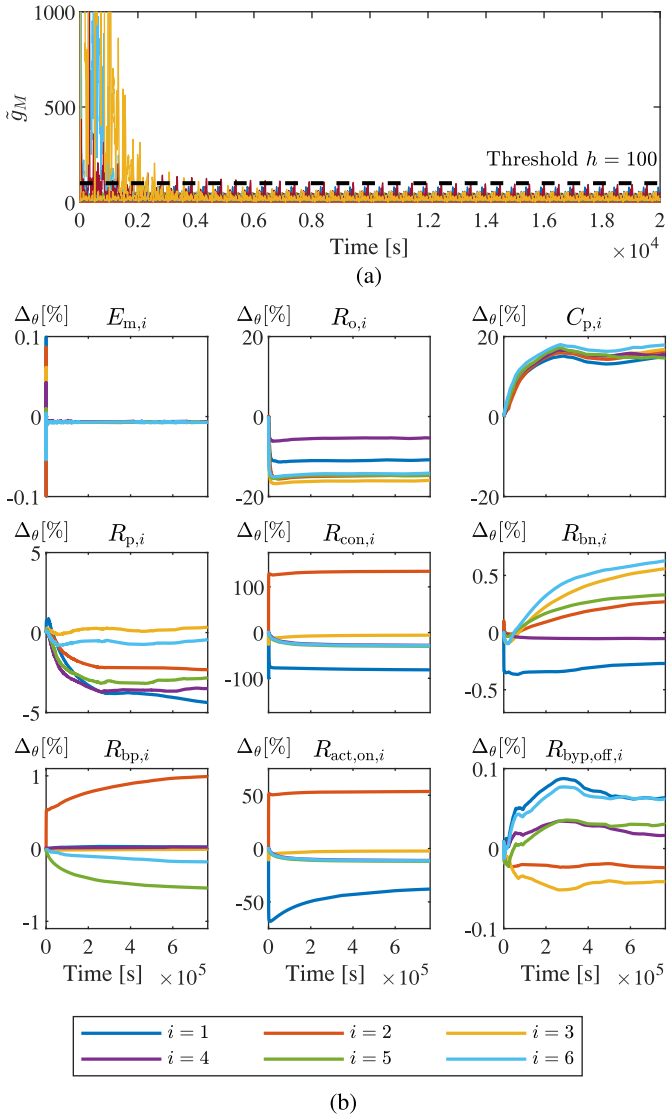

Fig. 9. Experimental results of the constrained parameter estimator. (a) Development of the residuals $\tilde{g}_M$ during the learning phase. (b) Percentage change of the parameters during the learning phase in relation to the initial parameters of Table IV.

to be about $2 \cdot R_{\mathrm{con},2}$ (about $7\,\mathrm{m}\Omega$ higher). This also affects the estimation of the resistance $R_{\mathrm{act,on},2}$ (about $1\mathrm{m}\Omega$ higher), because it is serial to the contact when the BS is open and is not measured by the voltage sensor (v_{cell} in Fig. 1). The busbar resistances ($R_{\mathrm{bn},i}$, $R_{\mathrm{bp},i}$) and the resistance differ $R_{\mathrm{byp,off},i}$ less than 1% from their initial values. The better the parameters of the residual generator fit to the battery system, the less artificial process noise needs to be added in the residual generator in order for the residuals to fluctuate around 0. The higher process noise in turn reduces the FDI precision.

3) Internal Short Circuit: Applying the algorithm from [31] to the present system, faults within the cell cannot be isolated given the present sensor set. Fig. 7 shows that by adding system knowledge, $R_{\mathrm{o},i}$ can be isolated from $E_{\mathrm{m},i}$. However, it is not possible to isolate $E_{\mathrm{m},i}$ from $R_{\mathrm{o},i}$ using passive FDI, even by adding system knowledge. Therefore, to show the benefits

TABLE IV
INITIAL PARAMETERS OF THE LEARNING PROCESS

	$E_{\mathrm{m},i}[0]$ [V]	$R_{\mathrm{o},i}[0]$ [mΩ]	$C_{\mathrm{p},i}[0]$ [F]	$R_{\mathrm{p},i}[0]$ [mΩ]
$i=1$	3.981	38.6	760	18.1
$i=2$	3.981	38.6	902	20.8
$i=3$	3.981	38.6	904	20.7
$i=4$	3.982	38.7	887	21.1
$i=5$	3.982	38.7	880	21.0
$i=6$	3.982	38.7	918	20.3
	$R_{\mathrm{con},i}[0]$	$R_{\{\mathrm{bp,bn}\},i}[0]$	$R_{\mathrm{act,on},i}[0]$	$R_{\mathrm{byp,off},i}[0]$
$i=1\ldots6$	5 mΩ	10 μΩ	2 mΩ	1 GΩ

of active fault diagnosis, a fault $f_{E_{\mathrm{m},6}}$ is emulated. Since the experimental setup in Fig. 8 does not provide access to internal cell variables, the fault $f_{E_{\mathrm{m},6}}$ is introduced by emulating an ISC. Fig. 10 shows the second row of the test setup. The first row contains no fault. In the second row, a $R_{\mathrm{ISC},6} = 3.37\,\Omega$ resistor is connected in parallel to cell $i = 6$. From the sensor perspective outside the cell, the resistor causes an instantaneous drop of the cell parameters $E_{\mathrm{m},6}$, $R_{\mathrm{o},6}$, and the state $v_{\mathrm{p},6}$ by the factor

$$c_f = \frac{R_{\mathrm{ISC},6}}{R_{\mathrm{ISC},6} + R_{\mathrm{o},6}} \approx 0.989. \tag{40}$$

Strictly speaking, an ISC emulated in this way contradicts the single-fault assumption. However, the internal resistance decreases by about $f_{R_{\mathrm{o},6}} \approx -0.39\,\mathrm{m}\Omega$. Thus, its change is clearly below the minimal detectable fault amplitude, as shown in Table II. Changes in the state $v_{\mathrm{p},6}$ show as cell-voltage fluctuations and therefore can be modeled by fluctuations in $E_{\mathrm{m},6}$. Consequently, since faults in the *RC*-element of the cell are not considered in the FDI framework, the vast majority of the emulated ISC causes a change in the open-circuit voltage $E_{\mathrm{m},6}$, thus replicating the desired fault. The change in $E_{\mathrm{m},6}$ is about $f_{E_{\mathrm{m},6}} \approx -38.4\,\mathrm{mV}$.

The results of the active FDI framework are shown in Fig. 11. The switch states for the second row are shown on the top of Fig. 11, followed by the probability for the two most likely faults, the normalized estimated fault amplitude, measured cell currents $i_{\mathrm{cell},i}$ and voltages $v_{\mathrm{cell},i}$, and the value of the residuals. The fault is introduced at $t = 610.8$ s and detected at $t = 612$ s due to the sampling rate of 1 Hz. A step in the cell currents $i_{\mathrm{cell},i}$ and cell voltages $v_{\mathrm{cell},i}$ indicates the introduction of the fault. Before switching, the probability for both faults $f_{E_{\mathrm{m},6}}$ and $f_{R_{\mathrm{o},6}}$ is 50% each. Thus, in case all cells are active (from $t = 0$s to $t = 849.8$ s), the fault $f_{E_{\mathrm{m},6}}$ is not isolable from the fault $f_{R_{\mathrm{o},6}}$ as also predicted by the simulations (see Fig. 7). At $t = 849.8$ s, the FDI algorithm proposes a new switch state, action $a_j[1]$. The active hypothesis testing policy determines that its best to take the cell $i = 6$ from the system, in order for both faults to be isolable. After switching all cells in the second row $i \in \{4, 5, 6\}$ into *Bypass* state, the respective cell currents are $i_{\mathrm{cell},4,5,6} = 0$ and the fault $f_{R_{\mathrm{o},6}}$ does not show in the system. However, it is observed that the cell voltages continue to decrease due to the ISC of cell $i = 6$. In the residuals $\mathbf{r}$, it is observed that the system is still faulty. Thus, leaving only the fault $f_{E_{\mathrm{m},6}}$ as a possibility. Consequently, the probability for the

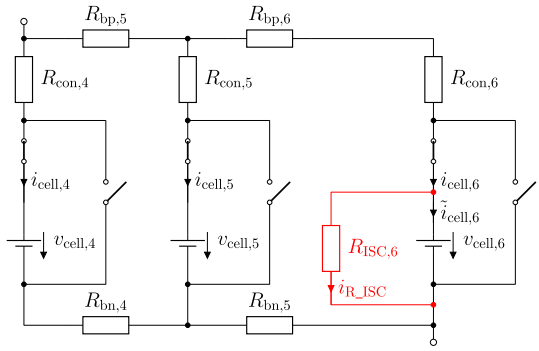

Fig. 10. Equivalent circuit of the second row of the experimental setup from Fig. 8. The ISC of cell $i = 6$ is emulated by adding a resistor R_{ISC}.

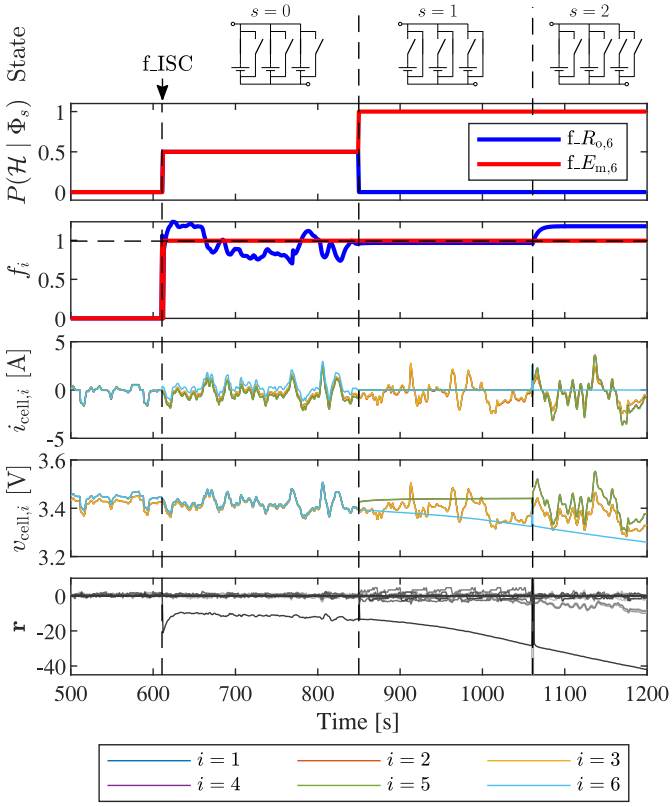

Fig. 11. Experimental results for the FDI of $f_{E_{\mathrm{m},6}}$. From top to bottom: switch states for the second row of RBS cells, probability for the two most likely faults, normalized estimated fault amplitude f_i, measured cell currents $i_{\mathrm{cell},i}$, measured cell voltages $v_{\mathrm{cell},i}$, and value of the residuals $\boldsymbol{r}$.

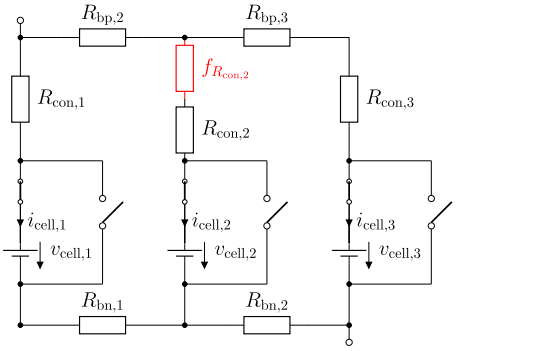

Fig. 12. Equivalent circuit of the first row of the experimental setup from Fig. 8. The increased contact resistance at cell $i = 2$ is emulated by an additional resistor $f_{R_{\mathrm{con},2}}$.

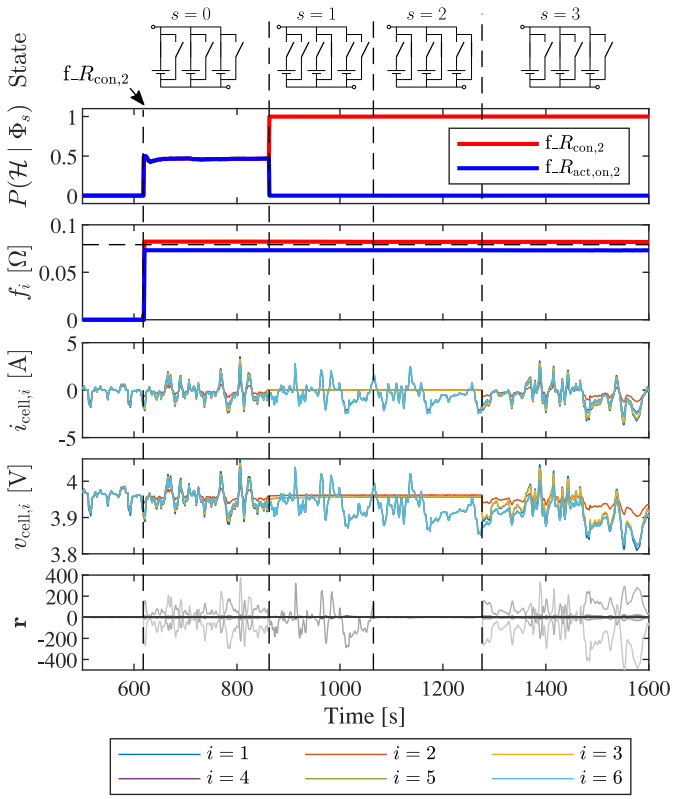

Fig. 13. Experimental results for the FDI of $f_{R_{\mathrm{con},2}}$. From top to bottom: switch states for the first row of RBS cells, probability for the two most likely faults, estimated fault amplitude f_i, measured cell currents $i_{\mathrm{cell},i}$, measured cell voltages $v_{\mathrm{cell},i}$, and value of the residuals $\boldsymbol{r}$.

fault $f_{E_{\mathrm{m},6}}$ increases to $P(\mathcal{H}_{E_{\mathrm{m}}} \mid \Phi_{0:1}) = 100\%$. At $t = 1061$ s the system switches again, with all cells except cell $i = 6$ in *Active* state. The results show, using the example of fault $f_{E_{\mathrm{m},6}}$ that the isolation capability is increased by active fault diagnosis through switches.

4) Increased Contact Resistance: Considering Fig. 7, another important case for validating active fault diagnosis is a fault in a contact resistance $f_{R_{\mathrm{con},i}}$ or the AS $f_{R_{\mathrm{act,on},i}}$. In the following, the fault $f_{R_{\mathrm{con},2}}$ concerning the contact between cell $i = 2$ and the busbar is investigated by increasing its resistance to $f_{R_{\mathrm{con},2}} = 71.9\ \mathrm{m\Omega}$ (see Fig. 12). This experimental test is also used to validate the detectability measure. The results of the active FDI algorithm for the increased contact resistance are shown in Fig. 13. The figure is structured analogous to Fig. 11. The fault is introduced at $t = 617.9$ s and is detected at 618 s due to the sampling rate of 1 Hz. The introduction of the fault is observed by a step in the cell currents $i_{\mathrm{cell},i}$ and cell voltages $v_{\mathrm{cell},i}$. The system is tested with all cells in *Active* state until $t = 862.5$ s. The probabilities for a fault in $R_{\mathrm{con},2}$ and $R_{\mathrm{act,on},2}$ are both 46.8%. The probabilities for all other faults are individually below 1%, and sum up the remaining 6.4%. At $t = 862.5$ s the active FDI policy decides to bypass the cell

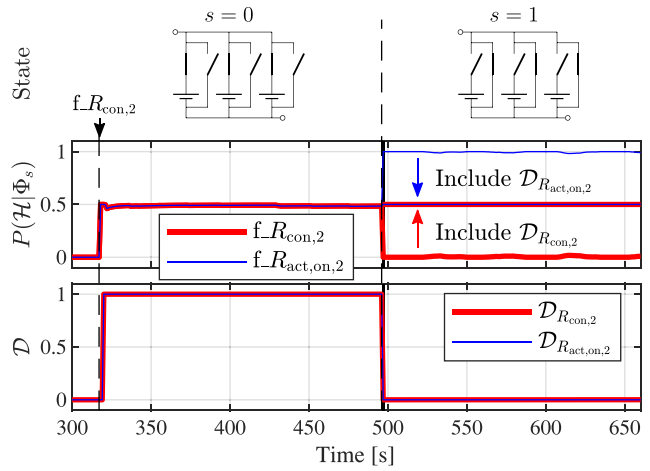

Fig. 14. Experimental results for the fault $f_{R_{\mathrm{con},2}} = 79.1\ \mathrm{m}\Omega$ introduced at $t = 317$ s. From top to bottom: switch states of the first row, decision of the active FDI algorithm with and without detectability measure, detectability measures of the faults.

$i = 2$ and opens the AS and BS for the cells $i \in 1, 3$ in order for the two faults to be isolable. After switching, the system is still faulty (see Fig. 13, **r**). A fault in $R_{\mathrm{act,on},2}$ would not show with the current switch state, thus the probability of a fault in $R_{\mathrm{con},2}$ rises to $P(\mathcal{H}_{R_{\mathrm{con},2}} \mid \Phi_{0:1}) = 99.85\%$. At $t = 1065$ s the algorithm switches all cells of the first row in *Bypass* state. Including the detectability measure (Definition IV.1), it is an expected behavior for a fault in $R_{\mathrm{con},2}$, thus its probability rises to $P(\mathcal{H}_{R_{\mathrm{con},2}} \mid \Phi_{0:2}) = 100\%$. Without the detectability measure, the fault would still be considered detectable. Thus, the probability for $f_{R_{\mathrm{con},2}}$ might fall as a consequence.

To further validate the detectability measure, all the cells of the first row are switched into *Bypass* state (switching action at $t = 1065$ s in Fig. 13) before the fault $f_{R_{\mathrm{con},2}}$ has been isolated. In this configuration, the fault in $R_{\mathrm{act,on},2}$ is structurally undetectable and the fault in $R_{\mathrm{con},2}$ is structurally but not analytically detectable. The poor analytical detectability is also observed in the residuals of Fig. 13 for $s = 2$. The residuals are close to zero during the period when the cells of the first row are in *Bypass* state. The experimental results with and without detectability measure are shown in Fig. 14. The switch positions are shown at the top. Underneath, the calculated fault probabilities of the active FDI algorithm with and without detectability measure is shown. At the bottom, the magnitude of the detectability measure is shown. Without a detectability measure, the algorithm for active fault isolation would incorrectly indicate the fault $f_{R_{\mathrm{act,on},2}}$. If, however, the detectability measure $\mathcal{D} \in [0, 1]$ according to Definition IV.1 is applied, both faults remain equiprobable since both faults are not analytically detectable after the switching action.

VI. Conclusion

In this article, a framework for active model-based FDI in RBS was presented. The framework consists of a residual-based constrained parameter estimator, a fault detection using a χ^2-test and a fault isolation using a fuzzy algorithm. The active fault isolation is based on active sequential hypothesis testing. A detectability measure was also introduced to increase robustness. The presented algorithms were validated simulatively and experimentally on a reconfigurable module of six lithium-ion cells in 2s3p configuration. The simulative investigations have shown that the active FDI is suitable to increase the confidence in detected faults. The addition of system knowledge, such as knowledge about the sign of a fault, increases the isolation properties. For the application under consideration, this results in an asymmetric isolation matrix. Active FDI using switches is suitable for isolating further faults. It has been shown that the minimum detectable fault amplitude significantly depends on the sensor quality. Secondarily, the minimum detectable fault amplitude is influenced by the sampling rate of the FDI framework. The sign of the fault has no influence on the minimal detectable fault amplitude within the considered application. The experimental results have shown that a parameter estimator is essential for the model-based FDI on the real system since the parameter values vary from cell to cell. In addition, the contact resistance between cell and busbar changes with each experimental setup. Without parameter estimation, the process noise of the model would have to be increased, which significantly reduces the FDI precision of the algorithm. Since many parameters were estimated, a constraint parameter estimator based on an SPKF with hard and soft constraints for the parameters was used. To demonstrate the advantages of active FDI, the framework was experimentally validated by emulating an ISC and an increased contact resistance. Both faults were correctly detected and isolated. The effectiveness of the introduced detectability measure, which increases robustness, was experimentally validated using the increased contact resistance.

The results have shown that in the considered system passive fault diagnosis algorithms already have good isolation properties due to the high number of sensors. However, the isolation properties are improved by active fault diagnosis, especially within the battery cell and between the cells. For this reason, active FDI is particularly promising for systems with fewer sensors or for reducing the number of sensors. Due to the preceding structural analysis, the presented framework is based on the single-fault assumption. However, since the active FDI framework does not rely on this limitation, the multifault application offers a promising extension of the framework. RBS offer the possibility to react to faults, for example, by bypassing a faulty cell. The presented FDI framework thus provides the basis for fault tolerance in RBS.

Acknowledgment

The authors would like to express their very great appreciation to Dr. M. Hinterberger (AUDI AG) for his constructive support and valuable expert advice during the planning and development of this article.

References

[1] T. Zimmermann, P. Keil, M. Hofmann, M. F. Horsche, S. Pichlmaier, and A. Jossen, "Review of system topologies for hybrid electrical energy storage systems," *J. Energy Storage*, vol. 8, pp. 78–90, 2016.

[2] S. Ci, N. Lin, and D. Wu, "Reconfigurable battery techniques and systems: A survey," *IEEE Access*, vol. 4, pp. 1175–1189, 2016.

[3] F. Helling, J. Glück, A. Singer, H.-J. Pfisterer, and T. Weyh, "The ac battery—A novel approach for integrating batteries into ac systems," *Int. J. Elect. Power Energy Syst.*, vol. 104, pp. 150–158, 2019.

[4] B. Liebhart, L. Komsiyska, and C. Endisch, "Passive impedance spectroscopy for monitoring lithium-ion battery cells during vehicle operation," *J. Power Sources*, vol. 449, 2020, Art. no. 227297.

[5] *Guide for the Use of Monitor Systems for Lead-Acid Traction Batteries*, IEC/TR 61431:1995, 1995.

[6] L. Lu, X. Han, J. Li, J. Hua, and M. Ouyang, "A review on the key issues for lithium-ion battery management in electric vehicles," *J. Power Sources*, vol. 226, pp. 272–288, 2013.

[7] N. Goto, S. Endo, T. Ishikawa, S. Tamura, Y. Shuto, and K. Tanaka, "Aircraft serious incident investigation report," Air Nippon Co., Ltd., 2014.

[8] G. J. Offer, V. Yufit, D. A. Howey, B. Wu, and N. P. Brandon, "Module design and fault diagnosis in electric vehicle batteries," *J. Power Sources*, vol. 206, pp. 383–392, 2012.

[9] S. Dey *et al.*, "Model-based real-time thermal fault diagnosis of lithium-ion batteries," *Control Eng. Pract.*, vol. 56, pp. 37–48, 2016.

[10] D. Schneider, U. Vögele, and C. Endisch, "Model-based sensor data fusion of quasi-redundant voltage and current measurements in a lithium-ion battery module," *J. Power Sources*, vol. 440, 2019, Art. no. 227156.

[11] S. Ci, J. Zhang, H. Sharif, and M. Alahmad, "Dynamic reconfigurable multi-cell battery: A novel approach to improve battery performance," in *Proc. 27th Annu. IEEE Appl. Power Electron. Conf. Expo.*, 2012, pp. 439–442.

[12] J. Armengol *et al.*, "Minimal structurally overdetermined sets for residual generation: A comparison of alternative approaches," *IFAC Proc. Vol.*, vol. 42, no. 8, pp. 1480–1485, 2009.

[13] Z. Liu, Q. Ahmed, J. Zhang, G. Rizzoni, and H. He, "Structural analysis based sensors fault detection and isolation of cylindrical lithium-ion batteries in automotive applications," *Control Eng. Pract.*, vol. 52, pp. 46–58, 2016.

[14] C. Zheng, Z. Chen, and D. Huang, "Fault diagnosis of voltage sensor and current sensor for lithium-ion battery pack using hybrid system modeling and unscented particle filter," *Energy*, vol. 191, 2020, Art. no. 116504.

[15] S. Dey, S. Mohon, P. Pisu, and B. Ayalew, "Sensor fault detection, isolation, and estimation in lithium-ion batteries," *IEEE Trans. Control Syst. Technol.*, vol. 24, no. 6, pp. 2141–2149, Nov. 2016.

[16] J. Xu, J. Wang, S. Li, and B. Cao, "A method to simultaneously detect the current sensor fault and estimate the state of energy for batteries in electric vehicles," *Sensors*, vol. 16, no. 8, pp. 1–15, 2016.

[17] R. Xiong, Q. Yu, W. Shen, C. Lin, and F. Sun, "A sensor fault diagnosis method for a lithium-ion battery pack in electric vehicles," *IEEE Trans. Power Electron.*, vol. 34, no. 10, pp. 9709–9718, Oct. 2019.

[18] Z. Liu and H. He, "Sensor fault detection and isolation for a lithium-ion battery pack in electric vehicles using adaptive extended Kalman filter," *Appl. Energy*, vol. 185, pp. 2033–2044, 2017.

[19] Z. Chen, K. Xu, J. Wei, and G. Dong, "Voltage fault detection for lithium-ion battery pack using local outlier factor," *Measurement*, vol. 146, pp. 544–556, 2019.

[20] W. Chen, W.-T. Chen, M. Saif, M.-F. Li, and H. Wu, "Simultaneous fault isolation and estimation of lithium-ion batteries via synthesized design of Luenberger and learning observers," *IEEE Trans. Control Syst. Technol.*, vol. 22, no. 1, pp. 290–298, Jan. 2014.

[21] N. Poulsen and H. Niemann, "Active fault diagnosis based on stochastic tests," *Int. J. Appl. Math. Comput. Sci.*, vol. 18, no. 4, pp. 487–496, 2008.

[22] A. Mesbah, S. Streif, R. Findeisen, and R. D. Braatz, "Active fault diagnosis for nonlinear systems with probabilistic uncertainties," *IFAC Proc. Vol.*, vol. 47, no. 3, pp. 7079–7084, 2014.

[23] H. Chernoff, "Sequential design of experiments," *Ann. Math. Statist.*, vol. 30, no. 3, pp. 755–770, 1959.

[24] S. Nitinawarat, G. K. Atia, and V. V. Veeravalli, "Controlled sensing for hypothesis testing," in *Proc. IEEE Int. Conf. Acoust., Speech, Signal Process.*, 2012, pp. 5277–5280.

[25] M. Naghshvar and T. Javidi, "Active sequential hypothesis testing," *Ann. Statist.*, vol. 41, no. 6, pp. 2703–2738, 2013.

[26] M. Naghshvar and T. Javidi, "Sequentiality and adaptivity gains in active hypothesis testing," *IEEE J. Sel. Topics Signal Process.*, vol. 7, no. 5, pp. 768–782, Oct. 2013.

[27] K. Cohen and Q. Zhao, "Active hypothesis testing for anomaly detection," *IEEE Trans. Inf. Theory*, vol. 61, no. 3, pp. 1432–1450, Mar. 2015.

[28] F. Ji, L. Liao, T. Wu, C. Chang, and M. Wang, "Self-reconfiguration batteries with stable voltage during the full cycle without the dc-dc converter," *J. Energy Storage*, vol. 28, 2020, Art. no. 101213.

[29] T. Bruen and J. Marco, "Modelling and experimental evaluation of parallel connected lithium ion cells for an electric vehicle battery system," *J. Power Sources*, vol. 310, pp. 91–101, 2016.

[30] D. Jung, H. Khorasgani, E. Frisk, M. Krysander, and G. Biswas, "Analysis of fault isolation assumptions when comparing model-based design approaches of diagnosis systems," *IFAC-PapersOnLine*, vol. 48, no. 21, pp. 1289–1296, 2015.

[31] M. Krysander, J. Aslund, and M. Nyberg, "An efficient algorithm for finding minimal overconstrained subsystems for model-based diagnosis," *IEEE Trans. Syst., Man, Cybern. A, Syst. Humans*, vol. 38, no. 1, pp. 197–206, Jan. 2008.

[32] V. A. Bavdekar, A. P. Deshpande, and S. C. Patwardhan, "Identification of process and measurement noise covariance for state and parameter estimation using extended Kalman filter," *J. Process Control*, vol. 21, no. 4, pp. 585–601, 2011.

[33] F. Gustafsson, "Statistical signal processing approaches to fault detection," *Annu. Rev. Control*, vol. 31, no. 1, pp. 41–54, 2007.

[34] A. Hagenblad, F. Gustafsson, and I. Klein, "A comparison of two methods for stochastic fault detection: The parity space approach and principal components analysis," *IFAC Proc. Vol.*, vol. 36, no. 16, pp. 1053–1058, 2003.

[35] J. George, "Robust fault detection and isolation in stochastic systems," *Int. J. Control*, vol. 85, no. 7, pp. 779–799, 2012.

[36] D. Jung, Y. Dong, E. Frisk, M. Krysander, and G. Biswas, "Sensor selection for fault diagnosis in uncertain systems," *Int. J. Control*, vol. 104, pp. 1–11, 2018.

[37] N. Mehranbod, M. Soroush, M. Piovoso, and B. A. Ogunnaike, "Probabilistic model for sensor fault detection and identification," *AIChE J.*, vol. 49, no. 7, pp. 1787–1802, 2003.

[38] L. D. Couto and M. Kinnaert, "Internal and sensor fault detection and isolation for li-ion batteries," *IFAC-PapersOnLine*, vol. 51, no. 24, pp. 1431–1438, 2018.

[39] M. Blanke, M. Kinnaert, J. Lunze, and M. Staroswiecki, *Diagnosis and Fault-Tolerant Control*. Berlin, Germany: Springer, 2016.

[40] R. van der Merwe and E. A. Wan, "The square-root unscented Kalman filter for state and parameter-estimation," in *Proc. IEEE Int. Conf. Acoust., Speech, Signal Process.*, 2001, pp. 3461–3464.

[41] G. L. Plett, "Sigma-point Kalman filtering for battery management systems of LiPB-based HEV battery packs," *J. Power Sources*, vol. 161, no. 2, pp. 1369–1384, 2006.

[42] Z. Chen, "Bayesian filtering: From Kalman filters to particle filters, and beyond," *Statistics*, vol. 182, pp. 1–69, Jan. 2003, doi: 10.1080/02331880309257.

[43] X. Zhang, W. Hu, Z. Zhao, Y.-G. Wang, X. Li, and Q. Wei, "SVD based Kalman particle filter for robust visual tracking," in *Proc. Int. Conf. Pattern Recognit.*, Tampa, FL, USA, 2008, pp. 1–4.

[44] D. Simon, "Kalman filtering with state constraints: A survey of linear and nonlinear algorithms," *IET Control Theory Appl.*, vol. 4, no. 8, pp. 1303–1318, 2010.

[45] S. Altmannshofer, C. Endisch, J. Martin, M. Gerngross, and R. Limbacher, "Robust estimation of vehicle longitudinal dynamics parameters," in *Proc. IEEE Intell. Veh. Symp.*, 2016, pp. 566–571.

[46] J. C. Bezdek, R. Ehrlich, and W. Full, "FCM: The fuzzy c-means clustering algorithm," *Comput. Geosci.*, vol. 10, no. 2/3, pp. 191–203, 1984.

[47] S. Miyamoto, K. Honda, and H. Ichihashi, *Algorithms for Fuzzy Clustering: Methods in c-Means Clustering With Applications* (Studies in Fuzziness and Soft Computing), vol. 229. Berlin, Germany: Springer, 2008.

[48] S. X. Ding, *Model-Based Fault Diagnosis Techniques*. London, U.K.: Springer, 2013.

[49] M. Naghshvar and T. Javidi, "Information utility in active sequential hypothesis testing," in *Proc. 48th Annu. Allerton Conf. Commun., Control, Comput.*, 2010, pp. 123–129.

[50] R. Isermann, *Fault-Diagnosis Systems: An Introduction From Fault Detection to Fault Tolerance*. Berlin, Germany: Springer, 2006.

[51] T. Zimmermann, M. Mora, S. Steinhorst, D. Mueller-Gritschneder, and A. Jossen, "Analysis of dissipative losses in modular reconfigurable energy storage systems using systemC TLM and systemC-AMS," *ACM Trans. Des. Autom. Electron. Syst.*, vol. 24, no. 4, pp. 1–33, 2019.

[52] "Worldwide harmonised light vehicles test procedure." [Online]. Available: http://www.unece.org/fileadmin/DAM/trans/doc/2012/wp29grpe/WLTP-DHC-12-07e.xls, on: May 1, 2020.

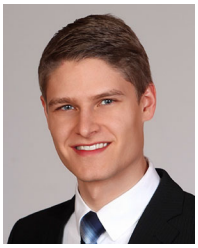

Michael Schmid was born in Germany. He received the B.Sc. and M.Sc. degrees in electrical and computer engineering, in 2014 and 2017, respectively, from the Technical University of Munich, Munich, Germany, where he is currently working toward the Ph.D. degree in electrical and computer engineering.

Since October 2017, he has been with the Institute of Innovative Mobility, Technische Hochschule Ingolstadt, Ingolstadt, Germany, where he is a Research Associate in a research project with the AUDI AG, Ingolstadt, Germany. His research interests include data-driven modeling, system identification, simulation and machine learning applied in battery systems.

Emanuel Gebauer was born in Buchloe, Germany, in 1995. He received the B.Sc. and M.Sc. degrees in electrical and computer engineering from the Technical University of Munich, Munich, Germany, in 2016 and 2020, respectively. He is currently working toward the Ph.D. degree in electrical and computer engineering as a Research Associate with the Institute of Innovative Mobility, Technische Hochschule Ingolstadt, Ingolstadt, Germany, in a research project with the AUDI AG.

Since March 2020, he has been a Research Associate with the Institute of Innovative Mobility, Technische Hochschule Ingolstadt, Ingolstadt, Germany, in a research project with the AUDI AG. His research interests include data-driven system modeling and identification, artificial intelligence applied to production optimization and fault diagnosis.

Christian Hanzl received the B.Eng. degree in electrical engineering and information technology from the Munich University of Applied Sciences, Munich, Germany, in 2016 and the M.Sc. degree in electrical and computer engineering from the Technical University of Munich, Munich, Germany, in 2018. He is currently working toward the Ph.D. degree in electrical and computer engineering with the Universität der Bundeswehr München, Munich, Germany.

Since 2018, he has been a Research Associate with the Institute of Innovative Mobility, Technische Hochschule Ingolstadt, Ingolstadt, Germany. His research interests include electronics development, power engineering, and semiconductors.

Christian Endisch (Member, IEEE) received the engineering degree and the Ph.D. degree in electrical engineering from the Technical University of Munich (TUM), Munich, Germany, in 2003 and 2009, respectively.

In 2010, he joined the AUDI AG, Ingolstadt, Germany, where he became a Project Manager in 2011. Since 2011, he has been researching and teaching in the field of artificial intelligence with the Chair for Electrical Drive Systems and Power Electronics, TUM. Since 2013, he has been with the Institute of Innovative Mobility (IIMo), Technische Hochschule Ingolstadt (THI), Ingolstadt, Germany, where he was appointed as a Professor in 2013 and a Research Professor in 2014. Since 2016, he has been the Head of the IIMo, THI. His research interests include learning battery systems, system identification, estimation procedures, optimization strategies, networked mobility, predictive operating strategies, innovative manufacturing and testing techniques with learning systems.